CO Oxidation on TiO₂ (110) Supported Subnanometer Gold Clusters: Size and Shape Effects

Lei Li,[†] Yi Gao,[‡] Hui Li,[†] Yu Zhao,[†] Yong Pei,*[,§] Zhongfang Chen,[∥] and Xiao Cheng Zeng*[,†]

[†]Department of Chemistry, University of Nebraska-Lincoln, Lincoln, Nebraska 68588, United States

[‡]Laboratory of Physical Biology and Division of Interfacial Water, Shanghai Institute of Applied Physics, Chinese Academy of Sciences, Shanghai, 201800, China

[§]Department of Chemistry, Key Laboratory of Environmentally Friendly Chemistry and Applications of Ministry of Education, Xiangtan University, Hunan Province 411105, China

[∥]Department of Chemistry, University of Puerto Rico, San Juan, Puerto Rico 00931

S *Supporting Information*

ABSTRACT: We performed a comprehensive study of catalytic activities of subnanometer Au clusters supported on $TiO_2(110)$ surface (Au_n/TiO_2, n = 1−4, 7, 16−20) by means of density functional theory (DFT) calculations and microkinetics analysis. The creditability of the chosen DFT/microkienetics methodologies was demonstrated by the very good agreement between predicted catalytic activities with experimental measurement (*J. Am. Chem. Soc*, **2004**, *126*, 5682−5483) for the Au_{1-4}/TiO_2 and Au_7/TiO_2 benchmark systems. For the first time, the size- and shape-dependent catalytic activities of the subnanometer Au clusters ($Au_{16}-Au_{20}$) on TiO_2 supports were systematically investigated. We found that catalytic activities of the Au_n/TiO_2 systems increase with the size n up to Au_{18}, for which the hollow-cage Au_{18} isomer exhibits highest activity for the CO oxidation, with a reaction rate ~30 times higher than that of Au_7/TiO_2 system. In stark contrast, the pyramidal isomer of Au_{18} exhibits much lower activity comparable to the Au_{3-4}/TiO_2 systems. Moreover, we found that the hollow-cage Au_{18} is robust upon the soft-landing with an impact velocity of 200 m/s to the TiO_2 substrate, and also exhibits thermal stability upon CO and O_2 co-adsorption. The larger pyramidal Au_{19} and Au_{20} clusters (on the TiO_2 support) display much lower reaction rates than the pyramidal Au_{18}. Results of rate of reactions for unsupported (gas-phase) and supported Au clusters can be correlated by a contour plot that illustrates the dependence of the reaction rates on the CO and O_2 adsorption energies. With the TiO_2 support, however, the catalytic activities can be greatly enhanced due to the weaker adsorption of CO on the TiO_2 support than on the Au clusters, thereby not only the ratio of O_2/CO adsorption energy and the probability for the O_2 to occupy the Ti sites are increased but also the requirement for meeting the critical line becomes weaker. The obtained contour plot not only can provide guidance for the theoretical investigation of catalytic activity on other metal cluster/support systems, but also assist experimental design of optimal metal cluster/support systems to achieve higher catalytic efficiency.
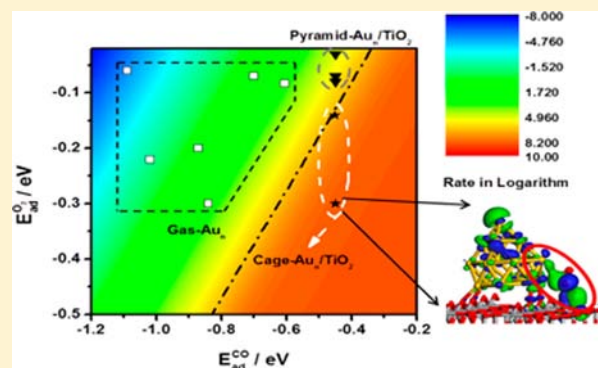
■ INTRODUCTION

Bulk gold is known to be catalytically inert for most heterogeneous reactions.[1] Amazingly, in 1987, Haruta et al. found that highly dispersed gold nanoparticles on a metal oxide support exhibit exceptional catalytic properties toward CO oxidation.[2] Since then, numerous experimental studies have shown that metal-oxide supported gold nanoparticles are active for numerous reactions, including CO oxidation,[2−6] propylene epoxidation[7] and the water-gas shift,[8,9] etc. Most recently, Haruta and co-workers reported application of nanogold catalyst in gas masks for oxidization of toxic chemicals, in bathrooms for removal of odor compounds,[10] or in vehicles for conversion of CO to CO_2.[11] However, limited understanding of the high catalytic activities of nanogold, particularly their size

and shape dependence, still hampers optimal design and synthesis of cost-effective catalysts for large-scale application.[12]

To understand the fundamental mechanism of the high catalytic activity, extensive experimental and computational efforts have been made to explore the most active sites on oxide-supported gold nanoparticles as well as the size and shape dependence.[6,13−16] For example, Haruta and co-workers reported that hemispherical Au particles perform better than spherical particles for catalyzing CO oxidation. They attributed this shape effect to the stronger interaction between the hemispherical gold nanoparticles and the underlying TiO_2

support.[6] Later, Goodman and co-workers observed that gold particles with 2−3 atomic layers and 2 nm in diameter exhibit the highest catalytic activities.[16] More recently, supported gold clusters with 5−10 atoms have been shown to give extremely high catalytic activity, but the gold clusters with less (or more) atoms are somewhat inert toward the thiophenol oxidation.[15] Theoretical studies have also shown that the CO oxidation is sensitive to the size of gold clusters, at least for the hollow-cage and pyramid gold clusters.[17,18]

Besides the shape and the size dependence, the role of the oxide support has been intensively investigated since the gold clusters on a different support can exhibit different catalytic activities. To date, several factors have been proposed to explain high catalytic activity of the supported Au clusters, such as the chemical structure of the support (including the defects),[6,8,19,20] charge transfer between Au clusters and the support, and the perimeter sites at the interface between Au clusters and the support. Haruta et al. suggested that gold clusters on reducible oxides are more active than irreducible oxides.[21] However, with the discovery of high catalytic activity of gold clusters on inert materials,[22] the reducibility of supports seems not a critical factor.

It is commonly believed that the charge transfer between the gold clusters and the support can be strongly affected by the surface structure.[23−25] Numerous experiments have shown that crucial species in gold catalysts are cationic gold atoms due to the formation of AuO_x or $AuO(OH)$ phase.[16,26−31] The existence of the cationic gold atoms in various systems is suggested to play an important role in the CO oxidation, such as in $Au/Mg(OH)_2$,[31] Au/MgO,[26,27] Au/CeO_2,[32] Au/TiO_2,[29] and $Au/\alpha\text{-}Fe_2O_3$[30] systems. On the other hand, defects on the support can lead to negatively charged Au clusters.[33,34] Yoon et al. reported that negatively charged Au_8 clusters on oxygen-vacancy F-centers of the MgO support are capable of catalyzing CO oxidation at the low temperature. In comparison, the clusters on the defect-free MgO surface are much less active.[24] More recently, Kim et al. performed DFT calculations and found that a supported Au_{13} can be negatively charged on partially reduced CeO_2 and exhibit notable catalytic activities toward the CO oxidation.[35]

The perimeter sites at the Au-support interface have been also suggested as the most active sites for CO oxidation.[36,37] Recently, Green et al. carried out a detailed experimental and theoretical study of the CO oxidation on the TiO_2 supported Au-nanowire. They revealed that at the perimeter sites the reaction barrier for the CO oxidation can be as low as ~0.16 eV.[37] Fujitani and Nakamura also indicated that the perimeter interface sites act as active sites at 320 K[38] and that at 400 K the turn over frequency (TOF) remains nearly constant, regardless of the mean diameter of Au clusters. The latter results suggest that mainly the surface sites of gold are responsible for the CO oxidation beyond 320 K. Goodman et al.[16] devised a planar bilayer gold on the support such that the reactants cannot directly interact with the support due to the coverage of the bilayer gold. In this system, therefore, the bilayer gold rather than the TiO_2 is solely responsible to high catalytic activity.

Our theoretical study is motivated by a recent review where Haruta and co-workers addressed the importance of understanding the catalytic activity of subnanometer gold clusters with precisely controlled size and shape.[39] Although catalytic activities of subnanometer gold clusters in the gas phase have been investigated,[40−43] few studies have addressed catalytic properties of the supported medium-sized gold clusters. In this

study, we focus on the subnanometer clusters in the size range from Au_{16} to Au_{20} (cf. Figure 1) due to the dramatic structural
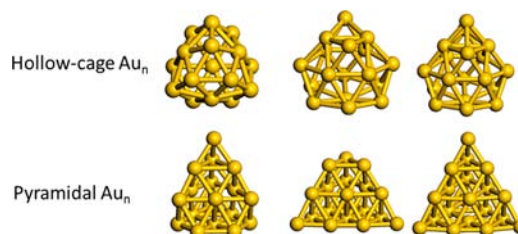
Figure 1. Optimized geometries of selected Au clusters: hollow-cages Au_{16}, Au_{17}, $Au_{18\text{-cage}}$ and pyramidal $Au_{18\text{-pyrd}}$, Au_{19}, Au_{20}.

transition in this size range (at least in the gas phase). In particular, Au_{16} is known to be a magic-number cluster and exhibits hollow-cage structure when carrying a negative charge in the gas phase. Au_{20} is another magic-number cluster and exhibits highly symmetric pyramidal (compact) structures in both neutral and anionic states. Au_{18} is a crossover cluster because it exhibits two distinctive stable isomers, i.e., the hollow-cage (cage-Au_{18}) and pyramid (pyrd-Au_{18}) when carrying a negative charge.[40,44] Another two gold clusters, Au_{17} and Au_{19}, exhibit hollow-cage and compact pyramidal structure, respectively. We show that the supported cage-Au_{18} exhibits higher catalytic activity than the pyrd-Au_{18} isomer due to the further enhanced O_2 adsorption onto the TiO_2 support.

Thus far, we are aware of only two previous theoretical studies that have reported detailed kinetic analysis of CO oxidation on Au sites, although all the Au sites were treated as equivalent sites.[35,45] In this study, we not only present a detailed kinetics analysis of the catalytic activity, especially for the reaction occurring near the Au-support interface, but also remove the equivalent-site assumption and take into account different chemical environment of Au atoms (such as different charge states and local cone angles) which can affect the adsorption energy of reactants[17] and yield site-dependent kinetics (e.g., reaction rate). We have also performed a comparative study of CO oxidation on Au_n/TiO_2 and the gas-phase Au_n. It shows that the catalytic activity can be greatly enhanced by a previously overlooked support effect, i.e., the weakened CO oxidation on the TiO_2 support can increase the ratio of O_2/CO adsorption energy, thereby lowering the requirement for meeting the critical line in the contour plot.

■ COMPUTATIONAL DETAILS

Structural Relaxation and CO Oxidation. The spin-unrestricted DFT (implemented in Dmol[3] 4.3 package) is employed within generalized-gradient approximation (GGA) in Perdew-Burke-Ernzerhof (PBE) form.[46,47] The real-space global cutoff radius is set to be 4.0 Å and only the Γ k-point is considered. Double numerical plus polarization (DNP) basis set and semicore pseudopotential are used to treat atomic orbitals and core electrons, respectively.[46,47] The transition-state search is performed using a combination of the linear and quadratic synchronous transit (LST/QST) method.[48,49] To neglect the interaction among the cluster and its periodic images, two large supercells (5 × 3 and 6 × 3) with 20 Å vacuum are used for the simulations of the TiO_2 supported cage-like and pyramidal Au clusters, respectively. The TiO_2 (110) slab has nine atomic layers, and the top-six atomic layers of TiO_2 are allowed to relax, while the bottom-three atomic layers are constraint to their lattice position. The convergence criteria for the geometrical optimization is 2 × 10⁻⁵ hartree for the energy change, 4 × 10⁻³ hartree/ Å for the gradient, and 5 × 10⁻³ Å for the displacement.

Adsorption energies of specific molecules i (i = CO and O_2) on the TiO_2-supported clusters Au_n and adsorption energies of the Au clusters on the TiO_2 (110) slab are computed based on the following two formulas:

$$E_{ad}^i = E_{i\text{-}Au_n/TiO_2} - E_{Au_n/TiO_2} - E_i \tag{1}$$

$$E_{ad}^{Au} = E_{Au_n/TiO_2} - E_{Au_n} - E_{TiO_2} \tag{2}$$

where E_{Au_n}, E_{TiO_2}, E_i and E_{Au_n/TiO_2} are the total energies of optimized bare Au_n, TiO_2 slab (per supercell), molecule i and TiO_2-supported Au_n, respectively; $E_{i\text{-}Au_n/TiO_2}$ is the total energy of the optimized molecule/cluster/support system i-Au_n/TiO_2, where molecule i is adsorbed on Au_n/TiO_2. In addition, as shown in Scheme 1, the

Scheme 1. Definition of Perimeter Sites and Surface Sites of TiO_2-Supported Au Clusters
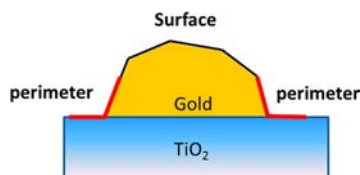
perimeter sites are defined to include Au atoms in the first or second Au layers next to TiO_2 as well as the five-fold Ti (Ti_{5f}) atoms near the Au-TiO_2 interface. Other Au atoms on the surface of Au clusters are viewed as surface sites.

Note that the Au or Ti sites for O_2 adsorption can be deactivated by the preoccupation of CO, thereby hindering the proceeding of the reaction. The competition of such inactive adsorption configuration is accounted for in the detailed microkinetics analysis (theoretical details are given in Part II of Supporting Information, SI). The adsorption energies of CO in the inactive adsorption configuration and O_2 in the active adsorption configuration (cf. equation 5 and 2 in Part II of SI, respectively) are denoted as $E_{ad}^{CO\ddagger}$ and $E_{ad}^{O_2\ddagger}$, respectively. The O_2 coverage on the active sites is determined by the ratio of $E_{ad}^{O_2\ddagger}$ to $E_{ad}^{CO\ddagger}$, referred to as the O_2/CO ratio. In other words, the O_2/CO ratio describes the capability of O_2 adsorption on either the active perimeter Ti_{5f} or the Au surface sites.

RESULTS AND DISCUSSION

Validation of the Method by Comparing with a Previous Experiment. To validate the theoretical method used in this study, we first examine catalytic activities of small-sized clusters Au_{1-4} and Au_7 on TiO_2 ($Au_{1-4, 7}$/TiO_2) (cf. Figure 2) for which experimental measurement of the rate of CO oxidation was reported by Lee et al.[50] Our calculations show that CO oxidation on Au_1/TiO_2 and Au_2/TiO_2 encounters a relatively high barrier of 0.65 and 1.14 eV, respectively (see Figure 2a). The high reaction barrier renders the Au_{1-2}/TiO_2 systems inactive to CO oxidation at the room temperature, consistent with the experimental results. In stark contrast, the Au_3/TiO_2 model system gives the lowest reaction barrier (0.26 eV), followed by Au_7/TiO_2 and Au_4/TiO_2 systems. Based on the computed reaction barrier alone, Au_3/TiO_2 is expected to exhibit the highest catalytic activity rather than Au_7/TiO_2, contrary to the experiment results.[50] Nevertheless, we notice that adsorption of O_2 is much stronger on Au_7/TiO_2 than on Au_3/TiO_2, indicating stronger capability to accommodate O_2. Therefore, Au_7/TiO_2 is expected to be more active than Au_3/TiO_2. Indeed, the detailed microkinetic analysis shows that Au_7/TiO_2 yields the highest reaction rate (7.6 × 10⁶ s⁻¹), followed by Au_3/TiO_2 and Au_4/TiO_2, whereas Au_1/TiO_2 and Au_2/TiO_2 are nearly inert due to negligible reaction rate

(see Figure 2b). The trend of catalytic activities predicted from the microkinetic analysis is in good agreement with experimental results,[50] confirming reliability of the kinetic analysis method used in this study.

CO Oxidation on TiO_2 Supported Hollow Cage Au_{16}, Au_{17}, Au_{18} and Pyramidal Au_{18}, Au_{19}, Au_{20}. $Au_{18\text{-cage}}$ and Au_{20} are prototype models for the hollow-cage and the pyramidal Au clusters, respectively. To assess activity of $Au_{18\text{-cage}}$/TiO_2 and Au_{20}/TiO_2 systems, multiple reaction pathways associated with the Au-surface sites and perimeter sites are investigated (cf. Figures S2–S6, Table S1). As illustrated in Part I of SI, the perimeter sites of both $Au_{18\text{-cage}}$/TiO_2 and Au_{20}/TiO_2 systems are the active sites to promote CO oxidation (cf. Figure S3c,d), following a dual-perimeter-site (DPS) mechanism. Here, CO adsorbed on the perimeter Au atom can be readily oxidized by the O_2 molecule adsorbed on the neighboring Ti_{5f} atom, and the reaction barrier is lower than 0.30 eV. As noted in Part I of SI, in the DPS mechanism, the bridge-adsorption configuration of the O_2 molecule is unfavorable because the nearest Au atom is occupied by the CO molecule.

To check if the DPS mechanism can be extended to other medium-sized Au clusters, we also examine CO oxidation on the TiO_2(110)-supported Au_{16}, Au_{17}, $Au_{18\text{-pyrd}}$, and Au_{19}. For comparison, the most favorable reaction pathways on the hollow-cage and pyramidal Au clusters (on the TiO_2 support) are displayed in Figures 3 and 4, respectively. Interestingly, for the Au_{17}/TiO_2, $Au_{18\text{-pyrd}}$/TiO_2, and Au_{19}/TiO_2 systems, the corresponding reaction barriers (under the DPS mechanism) are all lower than 0.3 eV, whereas Au_{16}/TiO_2 system entails a much higher energy barrier (0.62 eV). For the Au_{16}/TiO_2 and Au_{17}/TiO_2 systems, CO adsorbs at the perimeter Au atoms with the adsorption energy of −0.56 and −0.45 eV, respectively, close to that for the $Au_{18\text{-cage}}$/TiO_2 system. However, distinctive O_2 adsorption behavior is observed for the Au_{16}/TiO_2 system. As shown in the inset of Figure 3, adsorption of O_2 on the neighboring Ti_{5f} sites induces strong *structural deformation* of Au_{16} cage due to the strong interaction between the adsorbed O_2 and the Au atoms (cf. middle insets in Figure 3). The induced structural deformation raises the reaction barrier for the crossover of **TS1**, even though the strong O−Ti interaction still yields a low-energy barrier for **TS2**. Hence, for Au_{16}/TiO_2, the first step (**TS1**) is the rate-determining step rather than the O−O scission step. Differently, for the Au_{17}/TiO_2 system, upon the adsorption of CO on the perimeter Au site and O_2 adsorption at the neighboring Ti_{5f} site, little structural deformation is induced. The energy barriers associated with **TS1** and **TS2** are 0.05 and 0.24 eV, respectively, comparable to those for the $Au_{18\text{-cage}}$/TiO_2 system. Thus, Au_{17}/TiO_2 is expected to exhibit similar catalytic activities as $Au_{18\text{-cage}}$/TiO_2. In contrast, the perimeter sites in the Au_{16}/TiO_2 system may be viewed as inactive to the CO oxidation compared to the other two hollow-cage Au clusters. Such distinctive size effect is mainly due to structural flexibility of the Au_{16} cage.

Both Au_{16} and Au_{17} are hollow cages, while $Au_{18\text{-pyrd}}$ and Au_{19} are truncated pyramid. Thus, the TiO_2-supported $Au_{18\text{-pyrd}}$ and Au_{19} are expected to exhibit similar CO and O_2 adsorption behavior and more or less the same reaction barriers for CO oxidation. Indeed, as shown in Figure 4a,b, for $Au_{18\text{-pyrd}}$- and Au_{19}−TiO_2 systems, CO adsorption on Au surface sites near the interface results in similar adsorption energy, −0.74 and −0.75 eV. Moreover, the neighboring Ti_{5f} sites can adsorb O_2
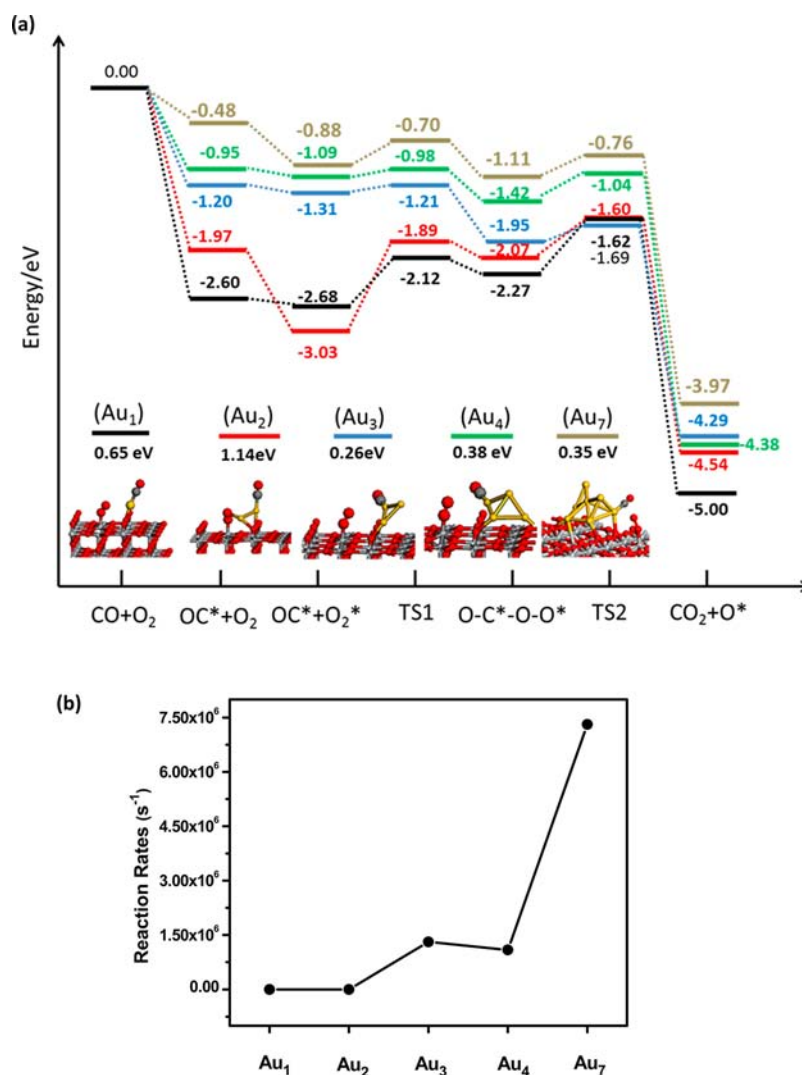
Figure 2. (a) Energy profile for CO oxidation on the TiO_2 supported Au_{1-4} and Au_7. The reaction barrier (eV) for the rate-limiting step is given for Au_{1-4} and Au_7 and the corresponding configuration in the initial state is shown in the insets. The symbol '*' refers to the atom or molecule or the intermediate being adsorbed on either the Au-cluster or the TiO_2 support. (b) Calculated reaction rates for different Au_n/TiO_2 systems ($n = 1-4$ and 7).

with nearly the same adsorption energy (-0.07 eV), in line with the experimentally characterized adsorption energy (-0.08 eV for O_2).[51] Upon the coadsorption of CO and O_2, the reaction encounters two reaction barriers whose heights are ∼0.10−0.12 and ∼0.28−0.29 eV for crossing the **TS1** and **TS2**, respectively. Hence, the adsorption of CO and O_2 on the perimeter sites of the $Au_{18\text{-pyrd}}/TiO_2$ and the Au_{19}/TiO_2 results in comparable adsorption energies as for Au_{20}/TiO_2. Moreover, the comparison of the two pathways for CO oxidation shows that the associated reaction barriers never exceed 0.30 eV for the two supported pyramidal Au_n.

In summary, the $Au_{16}-TiO_2$ interface results in a much higher reaction barrier of 0.62 eV due to the structural deformation. However, the reaction barriers below 0.3 eV are characterized as the TiO_2 supported Au_{17}, $Au_{18\text{-cage}}$, $Au_{18\text{-pyrd}}$, Au_{19}, and Au_{20}. It seems the catalytic activities of the supported subnanometer Au clusters are not critically dependent on the structure and size of Au clusters except Au_{16}. However, besides reaction barriers, CO and O_2 coverage is another important factor to affect the reaction rate of CO oxidation.

Size and Shape Dependence of the TiO_2-Supported Au_n (n = 1−4, 7, and 16−20). The computed reaction rates and associated parameters for CO oxidation on Au_{16-20}/TiO_2 systems are listed in Table 1. As expected, Au_{16}/TiO_2 yields the lowest reaction rate due to the high reaction barrier (0.62 eV). Moreover, the reaction rates computed for Au_{17-20}/TiO_2 systems seem more closely related to the adsorption energy ratio of O_2 to CO, in view of their small difference in reaction barrier (less than 0.05 eV). In Figure 5, the reaction rates versus the size of Au clusters for the Au_n/TiO_2 systems (n = 3, 4, 7, and 16−20) are plotted. Except the Au_{16}/TiO_2 system, the reaction rate increases with the size of the Au clusters considered up to n = 18. The two smallest clusters, Au_1/TiO_2 and Au_2/TiO_2, are incapable of catalyzing CO oxidation at room temperature. The reaction rate for the Au_{17}/TiO_2 system is ∼4 times higher than the Au_7/TiO_2 system, while the $Au_{18\text{-cage}}/TiO_2$ system yields ∼30 times higher reaction rate than Au_7/TiO_2 system. Hence, $Au_{18\text{-cage}}/TiO_2$ is the most active catalyst among systems considered in this study. As a demonstration of the shape effect, the $Au_{18\text{-pyrd}}/TiO_2$ system gives much lower reaction rate than the $Au_{18\text{-cage}}/TiO_2$ system
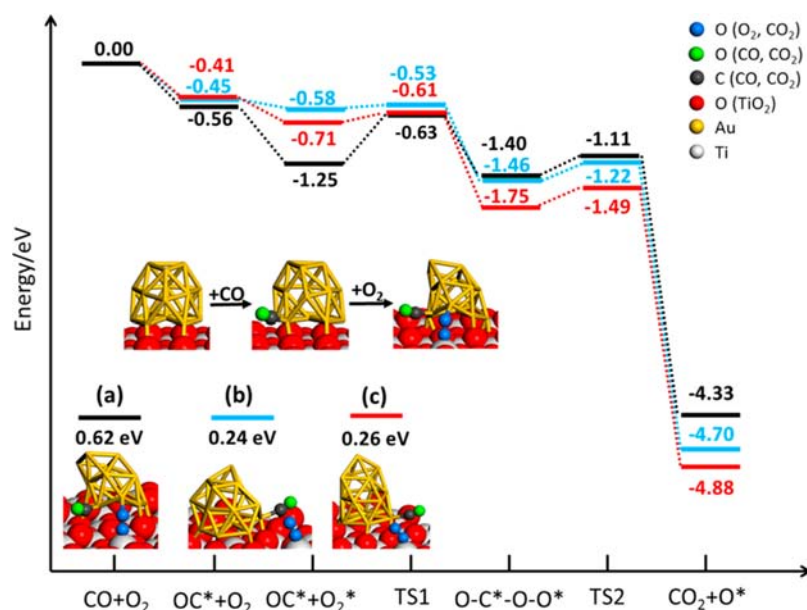
Figure 3. Computed most favorable reaction pathways for the CO oxidation at perimeter sites of hollow-cage Au_n/TiO_2 systems: (a) Au_{16}/TiO_2 (black lines), (b) Au_{17}/TiO_2 (blue lines), (c) $Au_{18\text{-cage}}/TiO_2$ (red lines). The reaction barrier (eV) for the rate-limiting step is given for (a−c), and the corresponding configuration in the initial state is shown in the lower insets. The middle insets illustrate the structural deformation of Au_{16} on the TiO_2 surface. The symbol * refers to the atom or molecule or the intermediate being adsorbed on either the Au-cluster or the TiO_2 support.
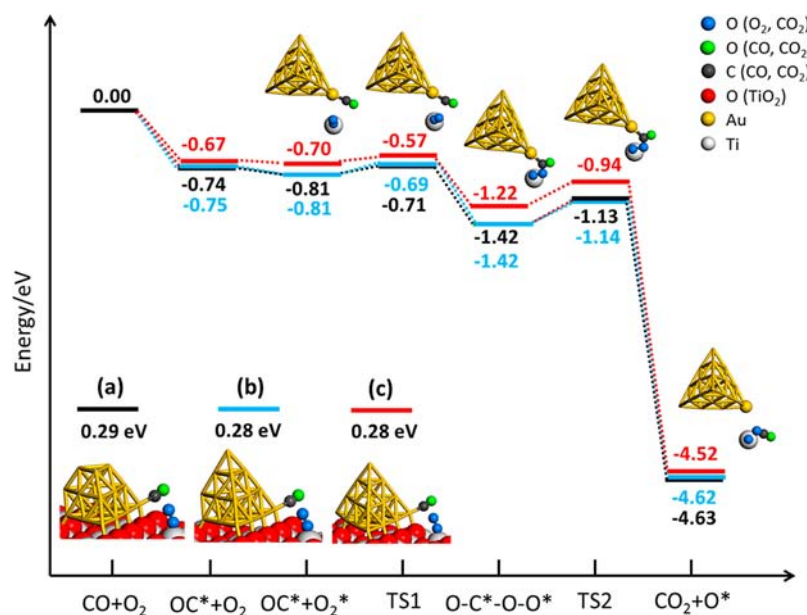
Figure 4. Computed most favorable reaction pathways for the CO oxidation at perimeter sites of pyramidal Au_n/TiO_2 systems: (a) $Au_{18\text{-pyrd}}/TiO_2$ (black lines), (b) Au_{19}/TiO_2 (blue lines), (c) Au_{20}/TiO_2 (red lines) . The reaction barrier (eV) for the rate-limiting step is given for (a−c), and the corresponding configuration in the initial state is shown in the lower insets. The upper inset (top view) illustrates configuration in pathway (c) (red lines). The symbol * refers to the atom or molecule or the intermediate being adsorbed on either the Au-cluster or the TiO_2 support.

(see Figure 5). In fact, the reaction rate for the $Au_{18\text{-pyrd}}/TiO_2$ is even lower than that of Au_4/TiO_2. On the other hand, for the slightly larger pyramidal clusters Au_{19} and Au_{20}, the reaction rates become lower than the $Au_{18\text{-pyrd}}/TiO_2$, demonstrating the importance of the size effect. These results also reveal that the supported hollow-cage Au clusters are more active than the pyramidal Au clusters. In summary, for the supported medium-sized Au clusters, the catalytic activities increase with the size of Au clusters until $n = 18$ where the cage-to-pyramidal structure transformation occurs.

Careful examination of the adsorption energy ratio of O_2 to CO (see Table 1) indicates that the enhancement of reaction rates on the supported hollow-cage Au clusters (Au_{17}/TiO_2 and Au_{18}/TiO_2) appears due to the increase of the O_2/CO ratio. As seen in Table 1, except the special case of Au_{16}/TiO_2, $Au_{18\text{-cage}}/TiO_2$ gives rise to the highest O_2/CO ratio (0.75), which leads to the highest O_2 coverage (∼0.016) and reaction rate. In contrast, much lower O_2 coverage on TiO_2 is seen for pyramidal-Au_n/TiO_2 due to very low O_2/CO ratio, hence much lower reaction rate. The Au_{20}/TiO_2 system gives rise to the lowest O_2/CO ratio (∼0.07), hence the lowest reaction rate.

Table 1. Computed Reaction Barriers of CO Oxidation at TS1 (E_a^{TS1}) and TS2 (E_a^{TS2}), Adsorption Energies of CO on the Perimeter Au Sites (E_{ad}^{CO}) and the Perimeter Ti$_{5f}$ Sites ($E_{ad}^{CO\ddagger}$), the Adsorption Energies of O$_2$ on the Perimeter Ti$_{5f}$ Sites ($E_{ad}^{O_2\ddagger}$), the O$_2$/CO Ratio of Adsorption Energy, O$_2$ Coverage ($\theta_{O_2\ddagger}$), and the Maximum Reaction Rates (R_1) on the Au$_n$/TiO$_2$ Systems[a]

	Au$_n$	E_a^{TS1}	E_a^{TS2}	E_{ad}^{CO}	$E_{ad}^{CO\ddagger}$	$E_{ad}^{O_2\ddagger}$	O$_2$/CO	$\theta_{O_2}^{\ddagger}$	R_1, s^{-1}
cage	Au$_{16}$	0.62	0.29	−0.56	−0.42	−0.69	1.64	9.89×10^{-1}	2.1×10^2
	Au$_{17}$	0.05	0.24	−0.45	−0.43	−0.14	0.33	4.66×10^{-4}	2.7×10^7
	Au$_{18\text{-cage}}$	0.10	0.26	−0.41	−0.40	−0.30	**0.75**	**1.63×10^{-2}**	**2.2×10^8**
pyramid	Au$_{18\text{-pyrd}}$	0.10	0.29	−0.74	−0.43	−0.07	0.16	3.28×10^{-6}	4.1×10^5
	Au$_{19}$	0.12	0.28	−0.75	−0.42	−0.06	0.14	3.28×10^{-6}	1.3×10^5
	Au$_{20}$	0.13	0.28	−0.67	−0.44	−0.03	0.07	4.71×10^{-7}	1.9×10^4

[a]The energy is in the unit eV, and the rate unit s^{-1} represents molecule per second.
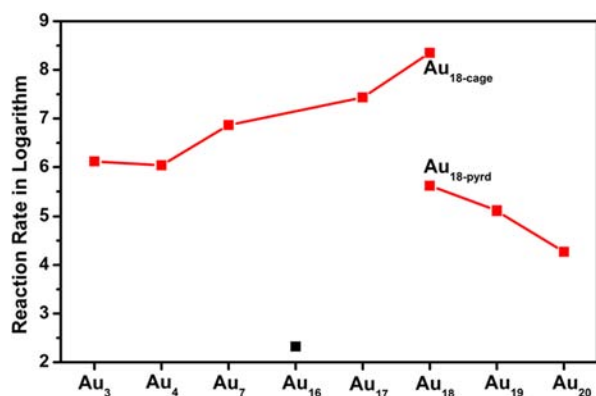
Figure 5. Calculated reaction rates (in logarithm value) versus the size of supported Au clusters for the Au$_n$/TiO$_2$ systems. The low reaction rate for Au$_{16}$/TiO$_2$ (a special case) is largely due to the strong structural deformation upon O$_2$ and CO adsorption.

We conclude that the weaker capability to accommodate O$_2$ for the pyramidal-Au$_n$/TiO$_2$ is responsible for their lower reaction rates, compared to the hollow-cage clusters.

To understand the origin of enhanced O$_2$ adsorption on hollow-cage-Au$_n$/TiO$_2$, we compute the molecular orbitals of the Au$_n$/TiO$_2$ systems upon the coadsorption of CO and O$_2$ and find that the stronger O$_2$ adsorption at the hollow-cage-Au$_n$-TiO$_2$ interface is attributed to the d-π orbital interaction between O$_2$ molecule and Au atom. As shown in Figure 6, for the hollow-cage-Au$_n$/TiO$_2$ systems, the adsorbed O$_2$ molecule leans to the Au clusters and interacts with the Au clusters through the overlap of O$_2$ π orbital and the Au d orbital. However, such d-π orbital overlap is not available for the pyramid-Au$_n$/TiO$_2$ systems. Thus, the d-π orbital interaction enables the stronger adsorption of O$_2$ at the hollow-cage-Au$_n$-TiO$_2$ interface, thereby increasing the O$_2$/CO ratio.

Born−Oppenheimer Molecular Dynamics Simulation of Soft-Landing on the TiO$_2$(110) Surface and Thermal Stability Test of Hollow-Cage Au$_{18}$ upon the Adsorption of CO and O$_2$. To examine stability of the Au$_{18\text{-cage}}$/TiO$_2$ system during the soft-landing process and upon the adsorption of CO and O$_2$, we perform a Born−Oppenheimer molecular dynamics (BOMD) simulation using the CP2K code.[52] The BOMD simulation is based on DFT in the form of PBE functional[53] and a mixed Gaussian and plane-wave (GPW) basis set with the Goedecker−Teter−Hutter (GTH) pseudopotential[54,55] adopted to describe the interaction between valence electrons and atomic cores. The plane-wave energy cutoff is 80 Ry. A relative large supercell (6 × 3) with vacuum distance of 15 Å is used so that the interactions among the cluster and its periodic images can be neglected. The supercell
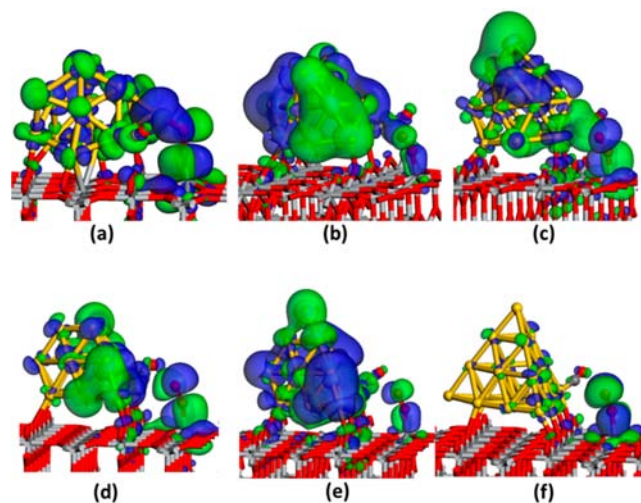
Figure 6. The fourth highest occupied molecule orbital (HOMO-4) for the coadsorbed CO and O$_2$ (at the initial state and under the DPS mechanism) on the Au$_n$/TiO$_2$ systems: (a) Au$_{16}$/TiO$_2$, (b) Au$_{17}$/TiO$_2$, (c) Au$_{18\text{-cage}}$/TiO$_2$, (d) Au$_{18\text{-pyrd}}$/TiO$_2$, (e) Au$_{19}$/TiO$_2$, (f) Au$_{20}$/TiO$_2$. The isosurface is set to be 0.015 e/Å^3. More molecular orbitals are displayed in Figure S8.

contains a (110)-terminated rutile TiO$_2$ slab (17.80 × 19.49 Å) with 12-atomic layers where the top-six atomic layers are free to relax during the simulation, while all atoms in the bottom-six atomic layers are fixed to their lattice position. Structures of Au clusters and TiO$_2$(110) surface are fully relaxed prior to the MD simulation. For the soft-landing simulation, the constant-energy and constant-volume (NVE) ensemble is selected with a time step of 1.0 fs, while for examining the thermal stability, the constant-temperature and constant-volume (NVT) ensemble is used with the temperature being controlled at 125 and 298 K, respectively.

In the soft-landing simulation, the Au$_{18\text{-cage}}$ cluster is initially placed 5.0 Å above the TiO$_2$(110) surface so that there is only weak dispersion interaction between the Au cluster and the TiO$_2$(110) surface. The initial relative velocity between the center of mass of the gold cluster and the TiO$_2$ substrate is ∼200 m/s (corresponding to ∼0.1 eV/atom, unit conversion refers to Sec. 3 in Part I of SI). Snapshots of the soft-landing at different time steps are shown in Figure 7a, while the full BOMD trajectory is shown in Movie S1. The Au$_{18\text{-cage}}$ starts to collide with the TiO$_2$ surface at ∼1.4 ps and is bounced backward at ∼2.8 ps. During the collision, the interconversion between the kinetic energy and internal energy is seen (Figure S9), and the overall hollow-cage structure of Au$_{18}$ exhibits little change, suggesting that the hollow-cage structure of Au$_{18}$ is
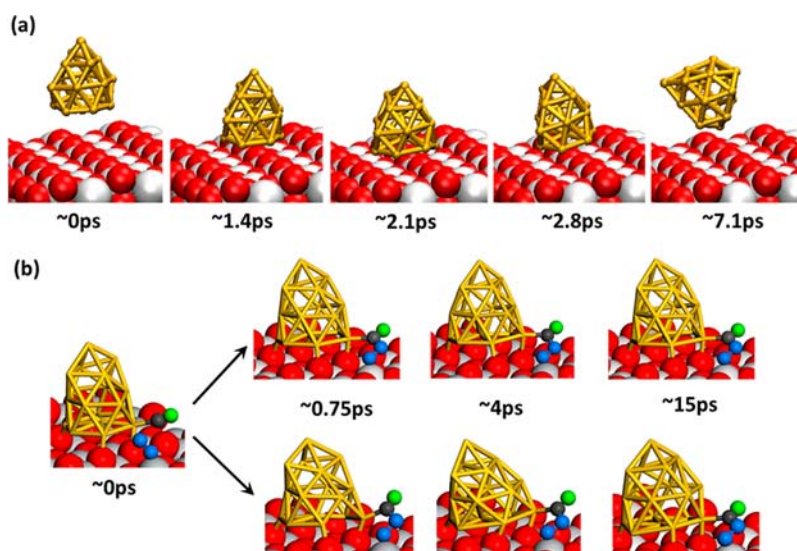
Figure 7. Snapshots of BOMD simulation at different time steps for (a) $Au_{18\text{-}cage}$ soft-landing onto $TiO_2(110)$ surface and (b) $Au_{18\text{-}cage}/TiO_2$ system at 125 K (middle images) and 298 K (bottom images).

Table 2. Computed Reaction Barriers of CO Oxidation at TS1 (E_a^{TS1}) and TS2 (E_a^{TS2}), Adsorption Energies of CO on the Au Sites (E_{ad}^{CO}) and Neighboring Au Sites ($E_{ad}^{CO\ddagger}$), Adsorption Energies of O_2 ($E_{ad}^{O_2\ddagger}$), the O_2/CO Ratio, Maximum Reaction Rates (R_1), and Rescaled Reaction Rates (R_2) on the Gas-Phase Au_n[a]

	Au_n	E_a^{TS1}	E_a^{TS2}	E_{ad}^{CO}	$E_{ad}^{CO\ddagger}$	$E_{ad}^{O_2\ddagger}$	O_2/CO	R_1, s^{-1}	R_2, s^{-1}
cage	Au_{16}	0.34	0.80	−0.96	−0.96	−0.06	0.06	5.4×10^{-12}	6.9×10^{-4}
	Au_{17}	0.40	0.19	−1.09	−0.60	−0.08	0.13	1.6×10^{-2}	8.3×10^{2}
	$Au_{18\text{-}cage}$	0.27	0.28	−0.95	−0.87	−0.20	0.23	7.1×10^{-3}	7.9×10^{1}
	$Au_{18\text{-}pyrd}$	0.35	0.56	−1.16	−1.02	−0.22	0.22	1.2×10^{-7}	3.4×10^{-2}
pyramid	Au_{19}	0.06	0.23	−0.84	−0.84	−0.3	0.36	3.9×10^{3}	8.3×10^{2}
	Au_{20}	0.12	0.44	−0.80	−0.70	−0.06	0.10	8.7×10^{-3}	1.7×10^{1}

[a]The energy is in the unit eV.

highly robust. Hence, in the realistic soft-landing experiment, even at a high impact velocity of ~200 m/s (or ~0.1 eV/atom), it is most likely that the Au_{18}-cage can still retain its gas-phase hollow-cage structure in the course of the collision. More surprisingly, for the pyramidal Au_{20} cluster, a recent experiment demonstrates that the overall high-symmetry structure can be retained even at the impact energy of 3 eV/atom.[56] So both $Au_{18\text{-}cage}$ and pyramidal Au_{20} clusters are expected to maintain their gas-phase global-minimum structures upon deposition to the $TiO_2(110)$ surface.

Figure 7b displays snapshots at different time steps of BOMD simulation for which two different temperatures are considered, 125 and 298 K. In both simulations (each for 15 ps), the Au_{18}-cage can retain the initial hollow-cage structure without showing major structure deformation. The calculated radial distribution function of Au–Au distance is shown in Figure S10a, where two peaks located at 2.85 and 4.80 Å can be seen. The first peak corresponds to the Au–Au bond length, while the second peak corresponds to the distance between the secondary nearest Au atoms. The calculated radial distribution function of C–O distance (cf. Figure S10b) exhibits a sharp peak at 1.37 Å, indicating the formation of the OC*OO* intermediate as shown in the snapshots (Figure 7b). The CO_2 formation is not observed within 15 ps of BOMD simulation, due to relatively high reaction barrier (~0.26 eV) in the O–O scission step. In summary, the $Au_{18\text{-}cage}/TiO_2$ system is predicted to be the most active for the CO oxidation, and

the hollow-cage structure is little changed upon CO and O_2 adsorption at the room temperature.

Effect of the TiO_2 (110) Support. To examine the effect of TiO_2 support, we investigate CO oxidation on the gas-phase Au_n and present the calculation results in Table 2. The computed reaction barriers on the gas-phase Au_n (including Au_{16}, Au_{17}, $Au_{18\text{-}pyrd}$, and Au_{20}) are mostly consistent with those reported previously.[17,45] For $Au_{18\text{-}cage}$ and Au_{19}, we find that the two Au–O linkages (TAOL) mechanism is more favorable as it gives lower barriers than those reported previously[17] (see Figure S11 for details). The maximum reaction rates R_1 stemming from the gas-phase Au_n are also given in Table 2. For convenience of discussion, we rescale the reaction rates for gas-phase Au_n according to adsorption energy of CO and O_2 on each cluster, but using the same reaction barrier that were computed from the $Au_{18\text{-}cage}$-TiO_2 system under the DPS mechanism (cf. Table 2). The rescaled reaction rates are named as R_2 (Table 2) and plotted in Figure 8a. With this scaling, the increase or decrease of R_2 relative to R_1 can be simply attributed to the change of reaction barrier, while the rate difference between R_2 associated with the gas-phase Au_n (open squares in Figure 8a) and R_2 associated with the supported Au_n (red circle in Figure 8a) can be mainly attributed to the O_2/CO ratio.

As shown in Figure 8b, the hollow-cage Au_{17} and Au_{18}, when deposited onto the TiO_2 support, give rise to a higher O_2/CO ratio than the corresponding gas-phase Au_n. Hence, the reaction rates associated with the Au_{17}/TiO_2 and $Au_{18\text{-}cage}/TiO_2$ are much higher than the rescaled reaction rates R_2 associated with
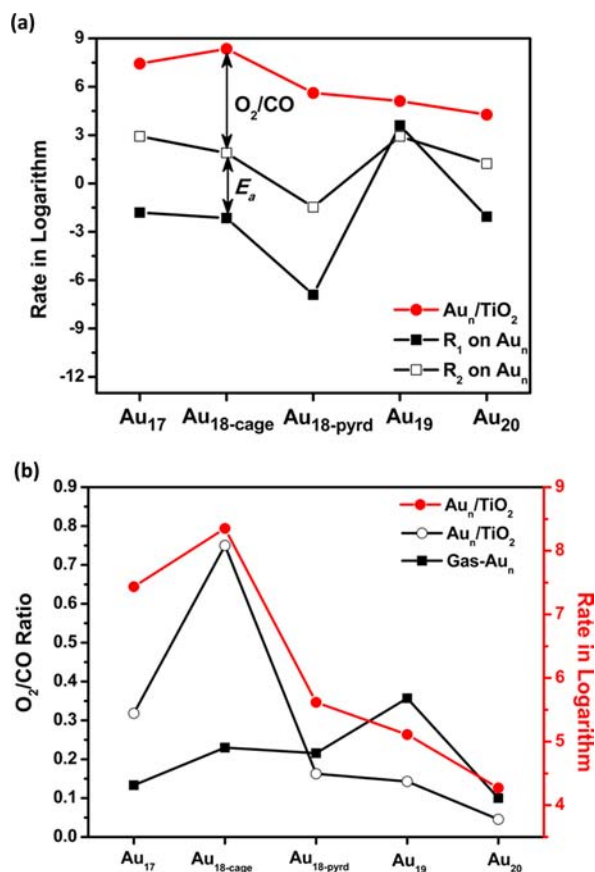
Figure 8. (a) Calculated reaction rates for different Au_n/TiO_2 (red lines) systems and gas-phase clusters Au_n (black lines). Note that R_1 and R_2 represent the actual and rescaled reaction rates on the gas-phase Au_n, respectively. The increment of R_2 relative to R_1 is due to the lowered reaction barriers E_a, while the O_2/CO ratio accounts for the rate difference in R_2 between the gas-phase Au_n and on Au_n/TiO_2. (b) Computed adsorption-energy ratio of O_2 to CO on the TiO_2 support for different Au_n/TiO_2 (open circle) and the gas-phase Au_n (black square) systems (left axis). Computed reaction rates (red circles) associated with different Au_n/TiO_2 systems are also shown (right axis) for demonstrating correlation between the rates and the adsorption-energy ratios.

the corresponding gas-phase Au_n. Furthermore, the Au-TiO_2 interface can provide active sites with lower reaction barriers, which would render R_2 higher than R_1. The higher reaction rates associated with the hollow-cage-Au_n/TiO_2 systems compared to the gas-phase counterparts can be attributed to two factors: lower reaction barrier and increased O_2/CO ratio. However, for the pyramidal Au clusters, the lowered reaction barrier and increased O_2/CO ratio are not sufficient to account for the high catalytic activity upon deposition onto TiO_2 support. As shown in Table 2, the gas-phase Au_{19} itself already has an exceptionally high reaction rate $3.9 \times 10^3 s^{-1}$, compared to other gas-phase Au_n. The exceptionally high reaction rate actually stems from the unique triangle Au sites on the truncated pyramidal corner as reported by Liu et al.[45] Such triangle sites can effectively decrease the reaction barrier to ~0.23 eV, which is even lower than typical barriers associated with the Au_n/TiO_2 systems. Moreover, such triangle sites can adsorb O_2 stronger, thus leading to the O_2/CO ratio (0.357) notably greater than that associated with the TiO_2 supported Au_{19}. Similarly, as shown in Figure 9b, both the gas-phase $Au_{18-pyrd}$ and Au_{20} are supposed to give higher rescaled reaction
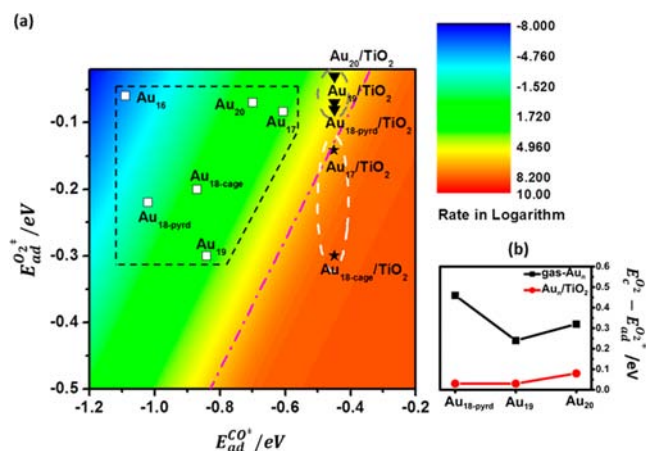
Figure 9. (a) Contour plot of reaction rates versus $CO(E_{ad}^{CO\ddagger})$ and $O_2(E_{ad}^{O_2\ddagger})$ adsorption energy. Open squares and black triangles and stars represent reaction rates on the gas-phase Au_n, pyramid-Au_n/TiO_2 and hollow-cage-Au_n/TiO_2, respectively. The dashed-dotted pink line refers to the designated critical line for which the reaction rate corresponds to $10^6 s^{-1}$. The dark-blue region refers to an unfavorable region where the weak adsorption of CO and O_2 would lead to high reaction barriers. (b) The difference between the actual O_2 adsorption energy ($E_{ad}^{O_2\ddagger}$) and the corresponding value taken from the critical line ($E_c^{O_2}$) for the gas-phase Au_n and Au_n/TiO_2 (n = 18-pyrd, 19, and 20) systems. Here, the value of $E_c^{O_2}$ is taken from the cross-point between the critical line (pink line in (a)) and the vertical line drawing from the interested point (e.g., an open square for gas-phase Au_n).

rates (R_2) because both show higher O_2/CO ratio than the corresponding supported Au_n. However, much lower reaction rates are obtained. Hence, further investigation is needed to understand effect of the TiO_2 support, which can lead to unexpected enhancement of catalytic activity of Au_n/TiO_2 (see below).

To gain more insights into the TiO_2-support effect, we depict a contour plot of reaction rates in logarithm versus CO and O_2 adsorption energy, as shown in Figure 9a. Note that the reaction rates in the contour plot are scaled (using the same reaction barrier for $Au_{18-cage}/TiO_2$) as described for the calculation of R_2. In Figure 9a, the reaction rates can be illustrated using four color schemes: blue (<-1.52), green (-1.52 to 4.00), yellow (4.00 to 6.00), and red (>6.00). The gas-phase Au_n is located at the blue or green region, whereas the pyramid-Au_n/TiO_2 and hollow-cage-Au_n/TiO_2 are located in yellow and red regions, respectively. Such a schematic plot illustrates the trend of catalytic activities as discussed above.

Different strategies are required to achieve high reaction rates for the gas-phase and the supported Au clusters, since they have distinctive CO adsorption energies. As shown in Figure 9a, at the boundary between the yellow and red region, a pink dash-dotted line is defined as the critical line on which the reaction rate reaches to a critical value $R_c = 10^6 s^{-1}$. Such reaction rates are comparable to those for the $Au_{3,4}/TiO_2$ and Au_7/TiO_2 systems, which have been experimentally measured. Using this critical line as a benchmark, we find that for a given CO adsorption energy value, the O_2 adsorption energy must reach a certain value to meet the critical line so that the reaction rate can be greater than R_c. Such a required O_2 adsorption energy is designated as a critical adsorption energy of O_2 ($E_c^{O_2}$).

For the gas-phase Au_n, the adsorption energy of O_2 is far from meeting the critical line (Figure 9a). In other words, the O_2/CO ratio is too small to meet the critical line, thus resulting

in low reaction rates. For example, CO is adsorbed onto the gas-phase Au_{19} with the adsorption energy -0.84 eV. Such adsorption energy requires the O_2/CO ratio of 0.60. However, the O_2/CO ratio for gas-phase Au_{19} is ~0.36, much smaller than the required O_2/CO ratio, hence resulting in much lower reaction rates despite of the low reaction barrier compared to the Au_{19}/TiO_2. Likewise, for another two gas-phase pyramidal Au_n, $Au_{18\text{-pyrd}}$, and Au_{20}, the required O_2/CO ratios are as high as 0.68 and 0.53 due to the adsorption energy of CO being -1.02 and -0.70 eV, respectively. Nevertheless, the O_2 adsorption energy is much weaker relative to the CO adsorption energy. Hence, the O_2/CO ratio (0.22 for $Au_{18\text{-pyrd}}$ and 0.10 for Au_{20}) is too low to reach the critical line, thus resulting in small reaction rates.

However, for the Au_n/TiO_2 system, CO adsorption energy on the TiO_2 surface decreases to ~ -0.43 eV. The required O_2/CO ratio for meeting the critical line drops to ~0.23, which can be achieved when the O_2 adsorption energy is as low as -0.10 eV. Although the O_2/CO ratio for pyramid-Au_n/TiO_2 is smaller than that for gas-phase Au_n (cf. Figure 7b), the difference between $(E_{ad}^{O_2\ddagger})$ and $(E_c^{O_2})$ is much smaller than that on the gas-phase Au_n due to the greatly reduced $E_c^{O_2}$, (Figure 9b), thus leading to higher reaction rates compared to the gas-phase Au_n. Furthermore, for the hollow-cage Au_{17}/TiO_2 and $Au_{18\text{-cage}}/TiO_2$, the d–$\pi$ orbital interaction between the adsorbed O_2 and Au clusters strengthen the adsorption of O_2, and thus they can accommodate O_2 with the adsorption energy -0.14 and -0.30 eV, respectively. The stronger O_2 adsorption relative to the required value enables meeting of the critical line as indicated in the contour map. Therefore, much higher reaction rates are expected for the Au_{17}/TiO_2 and $Au_{18\text{-cage}}/TiO_2$ systems compared to the gas-phase Au_n.

In summary, the TiO_2 support not only provides the active perimeter sites, but also lowers the requirement condition to meet the critical line.

■ CONCLUSION

We have studied the CO oxidation on the hollow-cage (Au_{16}, Au_{17}, $Au_{18\text{-cage}}$) and the pyramidal ($Au_{18\text{-pyrd}}$, Au_{19}, Au_{20}) Au clusters with and without the TiO_2 (110) support. Our systematical study indicates that the perimeter sites of Au-cluster/TiO_2 can significantly promote the CO oxidation. The peripherally adsorbed CO at a perimeter Au site can readily interact and react with a dangling O_2 on the neighboring Ti_{5f} site. Such a dual-perimeter-site mechanism typically results in a reaction barrier <0.3 eV for most supported Au clusters considered in this study, except Au_{16}/TiO_2. For the Au_{16}/TiO_2, the flexible cage structure tends to deform upon molecular adsorption, which raises the reaction barrier and renders the dual-perimeter-site mechanism unfavorable. To compare with previous experimental measurements, we have also examined catalytic activities of small-sized clusters Au_{1-4}/TiO_2 and Au_7/TiO_2 under the DPS mechanism. We find that the trend of activities predicted is in good agreement with the experimental one. Overall, the computed reaction rates for the Au_n/TiO_2 systems can be sensitively dependent on the size and shape of the supported Au clusters. As an example, for Au_{18} with both hollow-cage and pyramidal isomers, the cage isomer exhibits much higher catalytic activity than the pyramidal isomer largely because the second-layer Au atoms of the cage isomer (above the TiO_2 support) can enhance the adsorption of O_2 via the d–π orbital interaction on perimeter Ti sites. This enhance-

ment increases the ratio of O_2/CO adsorption energy, thereby the reaction rate.

More importantly, a schematic and useful contour plot of reaction rates is obtained from this comprehensive study. This contour plot can be used as guidance to predict optimal adsorption condition for CO and O_2 to achieve high reaction rates. In the contour plot, a critical line corresponding to the reaction rate of $R_c = 10^6/s$ is designated as a benchmark to determine optimal adsorption condition for CO and O_2 on the Au clusters or TiO_2 support. For a given value of CO adsorption energy, the O_2 adsorption must be strong enough so that the critical line can be met to achieve the reaction rate $>R_c = 10^6/s$. Without the TiO_2 support, the O_2 adsorption is typically weaker than the CO adsorption on the Au clusters (i.e., the ratio of O_2/CO adsorption energy is very low) so that the system cannot satisfy the condition for meeting the critical line. We find that the TiO_2 support can lower the requirement for the minimum value of O_2 adsorption energy to achieve high reaction rate due to the reduced CO adsorption energy on the perimeter Ti_{5f} sites (or increases the ratio of O_2/CO adsorption energy), in addition to the availability of active sites at the Au-TiO_2 interface. Finally, we expect that this contour plot approach is more generic and can be extended to analyze catalytic activities of other metal clusters/support systems.

In conclusion, we have systematically studied the size and shape dependence of catalytic properties of Au_n/TiO_2 system. We find that the TiO_2 substrate not only provides the active sites but also enhances the probability for the O_2 to occupy the Ti sites, thereby improving the catalytic activities for CO oxidation. The hollow-cage Au_{18} supported by $TiO_2(110)$ surface is predicted to be most active among the gold clusters considered for CO oxidation. Moreover, we find that the hollow-cage Au_{18} exhibits good stability during soft-landing process and thermal stability upon CO and O_2 coadsorption. Lastly, the obtained contour plot not only can provide guidance for the theoretical investigation of catalytic activity on other metal cluster/support systems, but also assist experimental design of optimal metal cluster/support systems to achieve higher catalytic efficiency.

■ ASSOCIATED CONTENT

Ⓢ Supporting Information

Detailed discussion about CO oxidation on $Au_{18\text{-cage}}/TiO_2$ and Au_{20}/TiO_2, including E-R and L-H mechanisms, a comparison of TAOL and SAOL mechanisms on the Au surface sites of $Au_{18\text{-cage}}/TiO_2$, computed reaction pathways and the variation of the bond length during CO oxidation at different perimeter sites and the removal of the second O atom, temperature and Kohn–Sham energy evolution and full-trajectory movie for $Au_{18\text{-cage}}$ soft-landing onto TiO_2 surface, radial distribution functions of Au–Au distance and C–O distance from BOMD simulation of the $Au_{18\text{-cage}}/TiO_2$ with the coadsorption of CO and O_2 at 125 and 298 K, the TAOL mechanism on the gas-phase $Au_{18\text{-cage}}$ and gas-phase Au_{19}, unit conversion for soft-landing speed, and the detailed microkinetic analysis. This material is available free of charge via the Internet at http://pubs.acs.org.

■ AUTHOR INFORMATION

Corresponding Authors
xzeng1@unl.edu
ypnku78@gmail.com

Notes

The authors declare no competing financial interest.

REFERENCES

(1) Hammer, B.; Norskov, J. K. *Nature* **1995**, *376*, 238−240.
(2) Haruta, M.; Kobayashi, T.; Sano, H.; Yamada, N. *Chem. Lett.* **1987**, 405−408.
(3) Valden, M.; Lai, X.; Goodman, D. W. *Science* **1998**, *281*, 1647−1650.
(4) Haruta, M.; Yamada, N.; Kobayashi, T.; Iijima, S. *Catal. Today* **1989**, *115*, 8.
(5) Xie, X. W.; Li, Y.; Liu, Z. Q.; Haruta, M.; Shen, W. J. *Nature* **2009**, *458*, 746−749.
(6) Fujikia, H.; Yamada, N.; Chijiiwaa, T.; Araia, S.; Tsubotab, S.; Haruta, M. *Catal. Today* **1997**, *36*, 9.
(7) Hayashi, T.; Tanaka, K.; Haruta, M. *J. Catal.* **1998**, *178*, 566−575.
(8) Boccuzzi, F.; Chiorino, A.; Manzoli, M.; Andreeva, D.; Tabakova, T. *J. Catal.* **1999**, *188*, 176−185.
(9) Williams, W. D.; Shekhar, M.; Lee, W. S.; Kispersky, V.; Delgass, W. N.; Ribeiro, F. H.; Kim, S. M.; Stach, E. A.; Miller, J. T.; Allard, L. F. *J. Am. Chem. Soc.* **2010**, *132*, 14018−14020.
(10) Ikegami, M.; Matsumoto, T.; Kobayashi, Y.; Jikihara, Y.; Nakayama, T.; Ohashi, H.; Honma, T.; Takei, T.; Haruta, M. *Appl. Catal., B* **2013**, *134*, 130−135.
(11) Peplow, M. *Nature* **2013**, *495*, S10−S11.
(12) Gates, B. C. *Chem Commun (Cambridge, U. K.)* **2013**, *49*, 7876−7877.
(13) Shekhar, M.; Wang, J.; Lee, W. S.; Williams, W. D.; Kim, S. M.; Stach, E. A.; Miller, J. T.; Delgass, W. N.; Ribeiro, F. H. *J. Am. Chem. Soc.* **2012**, *134*, 4700−4708.
(14) Tong, X.; Benz, L.; Kemper, P.; Metiu, H.; Bowers, M. T.; Buratto, S. K. *J. Am. Chem. Soc.* **2005**, *127*, 13516−13518.
(15) Corma, A.; Concepcion, P.; Boronat, M.; Sabater, M. J.; Navas, J.; Yacaman, M. J.; Larios, E.; Posadas, A.; Lopez-Quintela, M. A.; Buceta, D.; Mendoza, E.; Guilera, G. *Nat. Chem.* **2013**, *5*, 775−781.
(16) Chen, M. S.; Goodman, D. W. *Science* **2004**, *306*, 252−255.
(17) Gao, Y.; Shao, N.; Pei, Y.; Chen, Z. F.; Zeng, X. C. *ACS Nano* **2011**, *5*, 7818−7829.
(18) Gao, Y.; Shao, N.; Bulusu, S.; Zeng, X. C. *J. Phys. Chem. C* **2008**, *112*, 8234−8238.
(19) Schubert, M. M.; Hackenberg, S.; van Veen, A. C.; Muhler, M.; Plzak, V.; Behm, R. J. *J. Catal.* **2001**, *197*, 113−122.
(20) Comotti, M.; Li, W. C.; Spliethoff, B.; Schuth, F. *J. Am. Chem. Soc.* **2006**, *128*, 917−924.
(21) Haruta, M.; Tsubota, S.; Kobayashi, T.; Kageyama, H.; Genet, M. J.; Delmon, B. *J. Catal.* **1993**, *144*, 175−192.
(22) Turner, M.; Golovko, V. B.; Vaughan, O. P. H.; Abdulkin, P.; Berenguer-Murcia, A.; Tikhov, M. S.; Johnson, B. F. G.; Lambert, R. M. *Nature* **2008**, *454*, 981−984.
(23) Meyer, R.; Lemire, C.; Shaikhutdinov, S. K.; Freund, H. *Gold Bull.* **2004**, *37*, 72−124.
(24) Yoon, B.; Hakkinen, H.; Landman, U.; Worz, A. S.; Antonietti, J. M.; Abbet, S.; Judai, K.; Heiz, U. *Science* **2005**, *307*, 403−407.
(25) Remediakis, I. N.; Lopez, N.; Norskov, J. K. *Angew. Chem., Int. Ed.* **2005**, *44*, 1824−1826.
(26) Guzman, J.; Gates, B. C. *Angew. Chem., Int. Ed.* **2003**, *42*, 690−693.
(27) Guzman, J.; Gates, B. C. *J. Am. Chem. Soc.* **2004**, *126*, 2672−2673.
(28) Daniells, S. T.; Overweg, A. R.; Makkee, M.; Moulijn, J. A. *J. Catal.* **2005**, *230*, 52−65.
(29) Boyd, D.; Golunski, S.; Hearne, G. R.; Magadzu, T.; Mallick, K.; Raphulu, M. C.; Venugopal, A.; Scurrell, M. S. *Appl. Catal., A* **2005**, *292*, 76−81.
(30) Hutchings, G. J.; Hall, M. S.; Carley, A. F.; Landon, P.; Solsona, B. E.; Kiely, C. J.; Herzing, A.; Makkee, M.; Moulijn, J. A.; Overweg, A.; Fierro-Gonzalez, J. C.; Guzman, J.; Gates, B. C. *J. Catal.* **2006**, *242*, 71−81.
(31) Kobayashi, Y.; Nasu, S.; Tsubota, S.; Haruta, M. *Hyperfine Interact.* **2000**, *126*, 95−99.
(32) Guzman, J.; Carrettin, S.; Corma, A. *J. Am. Chem. Soc.* **2005**, *127*, 3286−3287.
(33) Chen, M. S.; Goodman, D. W. *Acc. Chem. Res.* **2006**, *39*, 739−746.
(34) Lopez, N.; Janssens, T. V. W.; Clausen, B. S.; Xu, Y.; Mavrikakis, M.; Bligaard, T.; Norskov, J. K. *J. Catal.* **2004**, *223*, 232−235.
(35) Kim, H. Y.; Lee, H. M.; Henkelman, G. *J. Am. Chem. Soc.* **2012**, *134*, 1560−1570.
(36) Haruta, M. *Catal. Today* **1997**, *36*, 153−166.
(37) Green, I. X.; Tang, W. J.; Neurock, M.; Yates, J. T. *Science* **2011**, *333*, 736−739.
(38) Fujitani, T.; Nakamura, I. *Angew. Chem., Int. Ed.* **2011**, *50*, 10144−10147.
(39) Takei, T.; Akita, T.; Nakamura, I.; Fujitani, T.; Okumura, M.; Okazaki, K.; Huang, J. H.; Ishida, T.; Haruta, M. *Adv. Catal.* **2012**, *55*, 1−126.
(40) Huang, W.; Bulusu, S.; Pal, R.; Zeng, X. C.; Wang, L. S. *ACS Nano* **2009**, *3*, 1225−1230.
(41) Bulusu, S.; Zeng, X. C. *J. Chem. Phys.* **2006**, *125*, 154303.
(42) Pal, R.; Wang, L. M.; Pei, Y.; Wang, L. S.; Zeng, X. C. *J. Am. Chem. Soc.* **2012**, *134*, 9438−9445.
(43) Huang, W.; Bulusu, S.; Pal, R.; Zeng, X. C.; Wang, L. S. *J. Chem. Phys.* **2009**, *131*, 234305.
(44) Bulusu, S.; Li, X.; Wang, L. S.; Zeng, X. C. *Proc. Natl. Acad. Sci. U.S.A.* **2006**, *103*, 8326−8330.
(45) Liu, C.; Tan, Y.; Lin, S.; Li, H.; Wu, X.; Li, L.; Pei, Y.; Zeng, X. C. *J. Am. Chem. Soc.* **2013**, *135*, 2583−2595.
(46) Delley, B. *J. Chem. Phys.* **1990**, *92*, 508−517.
(47) Delley, B. *J. Chem. Phys.* **2000**, *113*, 7756−7764.
(48) Halgren, T. A.; Lipscomb, W. N. *Chem. Phys. Lett.* **1977**, *49*, 225−232.
(49) Peng, C. Y.; Schlegel, H. B. *Isr. J. Chem.* **1993**, *33*, 449−454.
(50) Lee, S. S.; Fan, C. Y.; Wu, T. P.; Anderson, S. L. *J. Am. Chem. Soc.* **2004**, *126*, 5682−5683.
(51) Long, C. G.; Gilbertson, J. D.; Vijayaraghavan, G.; Stevenson, K. J.; Pursell, C. J.; Chandler, B. D. *J. Am. Chem. Soc.* **2008**, *130*, 10103−10115.
(52) The CP2K developers group 2004.
(53) Perdew, J. P.; Burke, K.; Ernzerhof, M. *Phys. Rev. Lett.* **1996**, *77*, 3865−3868.
(54) Goedecker, S.; Teter, M.; Hutter, J. *Phys. Rev. B* **1996**, *54*, 1703−1710.

(55) Hartwigsen, C.; Goedecker, S.; Hutter, J. *Phys. Rev. B* **1998**, *58*, 3641−3662.
(56) Wang, Z. W.; Palmer, R. E. *Nanoscale* **2012**, *4*, 4947−4949.

19346

dx.doi.org/10.1021/ja410292s | *J. Am. Chem. Soc.* 2013, 135, 19336−19346